

Trends in Satellite Sensors and Image Time Series Processing Methods for Crop Phenology Monitoring



Luca Pipia, Santiago Belda, Belen Franch, and Jochem Verrelst

1 Introduction

Agricultural production undergoes increasing pressure from anthropogenically-induced and natural changes, including rising population, conversion of food (cereals) into biofuels, increased protein demands and climatic extremes [1]. Through a fleet of Earth Observation (EO) satellites, National and International space agencies are determined to keep their fingers on the pulse of agricultural land and crop growth [2]. Among the objectives of the multiple EO satellite missions launched in the last five decades, primary importance has been given to observe agricultural and natural vegetation land covers [3–7]. The strong correlation between the response of vegetation in the visible and near-infrared spectrum and its biophysical activities led the preference towards optical sensors for crop growth monitoring [8].

Optical data from EO image time series at high temporal resolution can effectively assist in vegetation monitoring over time as they provide key information about vegetation status over large areas. However, imagery acquired at a high temporal resolution goes traditionally at the expense of a low spatial resolution, and EO missions dedicated to time series studies have long been restricted to the domain of wide swath that achieve global coverage on a near daily basis. For instance, the

L. Pipia

Institut Cartogràfic i Geològic de Catalunya (ICGC), Parc de Montjuïc,
Barcelona, Spain

Image Processing Laboratory (IPL), Universitat de València. C/Catedrático José Beltrán,
Paterna, Valencia, Spain

S. Belda · B. Franch · J. Verrelst (✉)

Image Processing Laboratory (IPL), Universitat de València. C/Catedrático José Beltrán,
Paterna, Valencia, Spain

e-mail: jochem.verrelst@uv.es

Advanced Very High-Resolution Radiometer (AVHRR) was pioneering in time series studies for vegetation monitoring studies at regional to global scales for more than 25 years. AVHRR has been collecting a near-daily global coverage of coarse-to-moderate spatial resolution (1 km and 8 km) providing a consistent time-series of temporally-composited observations [9–11]. As a marked improvement, the Moderate Resolution Imaging Spectrometer (MODIS) has provided, since the early 2000s, an improved times-series of multispectral observations, acquiring a global coverage of multispectral imagery with a high temporal (daily) resolution, a higher spatial resolution (250–500 m) and seven land-related spectral bands for vegetation detection. MODIS data have become increasingly used for vegetation growth monitoring over large geographic regions [12, 13]. Yet, probably the most noteworthy pioneering mission for land applications is the Landsat series of satellite-based sensors. Landsat has long been appropriate for many landscape characterization applications such as land cover classification, change detection and vegetation monitoring. It has a nominal 16-day temporal resolution and up to 30 m spatial resolution, with a data archive extending from the early 1970s to present. However, the usage of Landsat time series for crop growth monitoring has limitations because vegetation changes may occur more rapidly than the 16-day revisit time of Landsat. In addition, cloud cover contamination of the optical satellite observations further reduces the number of Landsat images available to adequately detect many seasonal events [8].

These pioneering monitoring missions paved the path for a diversity of dedicated EO land missions initiated by National and International space agencies with emphasis in exploiting the spatial, spectral, or temporal domain. With current and upcoming EO satellite missions, an ever-increasing amount of optical EO satellites are orbiting around the Earth, such as the Sentinel constellations on behalf of the joint ESA/European Commission initiative Copernicus and the NASA A-Train satellite constellations. With the operational super-spectral Copernicus' Sentinel-2 (S2) [14] and Sentinel-3 missions [15], as well as the recently launched and upcoming imaging spectrometer missions [16–19], an unprecedented data stream for vegetation mapping and monitoring becomes available. For instance, the unprecedented frequency of S2 multispectral observations (every five days) with a spatial resolution of 20 m (up to 10 m for specific bands) captures rapid changes of agricultural land-cover from national to field scale, serving as a major support for environmental monitoring and agricultural subsidy control [14]. Hence, S2 time series allows for high-resolution coverage of large areas with systematic data acquisition with high-frequency sampling during critical phases of the crop growth cycle [20]. The Sentinel-3 satellites even enable a short revisit time of less than two days for the optical sensor OLCI (Ocean and Land Colour Instrument), but it is a medium-resolution imaging spectrometer as it provides a spatial resolution of 300 m [15], and thus is less suited for crop monitoring at field scale.

Having an unprecedented influx of optical time series data at disposal, an essential condition for using image data for further processing is that it requires to be spatially and temporally continuous, i.e., gap-free data. Unfortunately, in

reality this need is often unfulfilled, due to multiple causes: (1) inadequate climatic conditions (clouds, snow, dust and aerosols), (2) instrumentation errors, (3) losses of data during data transmission or (4) low temporal resolution (i.e., long time needed to revisit and acquire data for the exact same location), among others. The causes above degrade the availability of spatial and temporal information required to retrieve land surface properties. Therefore, the impact of missing data on quantitative research can be serious, leading to biased estimates of parameters, loss of information, decreased statistical power, increased standard errors, and weakened findings [21]. For this reason, spatiotemporal reconstruction of gapped areas from satellite imagery is becoming crucial for monitoring purposes [22], including the knowledge of the life cycle of vegetation, i.e., vegetation phenology [23].

Another important remark is that, from an EO perspective, specific plant seasonal events such as budbreak, leaf out, leaf senescence, flowering and maturity of cereal crops cannot be directly detected at the spatial resolution of satellite imagery. Instead, more general descriptors of vegetation dynamics termed ‘land surface phenology (LSP)’ are calculated [8]. LSP refers to the seasonal pattern of variation in vegetated land surfaces observed from remote sensing [24]. This is distinct from observations of individual plants or species, as space-based observations aggregate information on the timing of heterogeneous vegetation development over pixel-sized areas. This aggregation often disassociates the response signal of the landscape from that of the individual species; yet is important for representing landscape scale processes in biosphere atmosphere interaction and crop monitoring models [24]. LSP metrics are typically associated with general inter-annual vegetation changes interpretable from spectral remote sensing imagery such as start of greening/season (SOS), the peak of growing season, onset of senescence or end of the season (EOS), and growing season length [24, 25], as well as other transition stages (e.g., maturity and senescence) [5]. Therefore, this chapter provides an overview of the possibilities for calculation of these LSP metrics from time series images for crop monitoring purposes.

Altogether, when aiming to process time series data for calculation of LSP metrics and agricultural monitoring purposes, a critical aspect to deal with is that EO data is spatially and temporally discontinuous. This implies that the ability to process irregular time series becomes indispensable for studying seasonal vegetation patterns. In this respect, this chapter aims to provide a general overview on agricultural land monitoring by means of EO image time series analysis and subsequent LSP calculation. To do so, first an historical overview of EO satellites with optical sensors that are designed to monitor the phenology of agricultural lands is given. Second, solutions are offered on how to gap-fill time series image data and then to calculate LSP metrics. Third, the calculation of LSP metrics from MODIS and 1 km aggregated S2 data is presented for two demonstration areas characterized by different dominant crop: corn and winter wheat. Finally, trends in EO missions and image time series processing are being discussed in the broader context of monitoring croplands’ phenology.

2 Satellite Sensors for Crop Phenology Monitoring

Although in the current era of EO missions time series processing has become standard practice in agriculture monitoring, it only recently reached maturity. Almost half a century was dedicated to overcoming challenges related to EO technology and optimizing for ideal temporal and spatial resolution. In this respect, this section intends to give a brief historical overview about EO satellite missions for agricultural monitoring purposes. Afterwards, time series data from NASA and ESA flagship missions for land applications are used for presenting crop monitoring demonstration cases.

When EO satellites were first available in the 60s, it was recognized that the technology held considerable promise for agricultural monitoring [26]. NASA was pioneering with EO programs for agricultural monitoring purposes. Initial efforts involved the NASA LACIE and AgriSTARS programs in the 70s. They made significant advances in crop monitoring but were seriously constrained by satellite data availability. At the beginning of EO missions, satellite optical data have been primarily provided globally at coarse-resolution (c. 250 m–8 km) by systems specifically developed for land applications. This is especially true for the AVHRR sensors, launched back in the 80s. AVHRRs provided daily global observations, which represent one of the most critical features needed for agriculture monitoring, but they were limited by their low spatial resolution (1 km). It has long been recognized that when working on agriculture applications, a good temporal resolution is required, given that the crop phenology and conditions (e.g., water supply, pests, environmental) can change very quickly. To this end, the NASA Long Term Data Record (LTDR) contains gridded daily surface reflectance and brightness temperatures derived from processing of the data acquired by the AVHRR sensors onboard four NOAA polar-orbiting satellites: NOAA-7, -9, -11 and -14. The Version 4 contains improvements to geolocation, cloud masking and calibration, making the data record suitable for crop monitoring [27]. This product is still operational, and its usefulness has been demonstrated for a wide variety of applications such as snow cover estimation [28], agricultural modeling [27], Leaf Area Index (LAI) and Fraction of Absorbed Photosynthetically Active Radiation (FAPAR) retrieval [29, 30], global vegetation monitoring [31, 32], burned area mapping [33] and albedo estimation products [34].

A next milestone involved the MODIS sensor on the Terra satellite. Since its launch in 2000, observations from the EOS/MODIS sensors have several of the key qualities needed for global agriculture monitoring such as global, daily coverage at coarse spatial resolution (250 m) and a suite of validated products. With MODIS onboard Terra (morning satellite) and Aqua (afternoon satellite) getting to the end of its operational life, it was high time to transition into new satellites. The Visible Infrared Imaging Radiometer Suite (VIIRS) onboard the Suomi National Polar-orbiting Partnership (S-NPP) satellite provided continuity with MODIS from 2012 [35, 36]. It overpasses once a day and during the afternoon, which decreases the chance of getting cloud-free observations, especially in the tropical regions.

However, the combination with the ESA Sentinel-3 satellite, that overpasses during the morning and has similar characteristics to MODIS, provides continuity to the successful and still valuable (due to its high temporal resolution) coarse resolution missions. Despite the advantage of the high revisit time, the main disadvantage of coarse to moderate resolution sensors is the spatial resolution that often mixes, in a given pixel, signals from different land cover types and crops. Stratifying a region into different crop types (commonly termed as crop masking) is an important step in developing EO-based agriculture models [37]. Such masks enable the isolation of the remotely sensed, crop-specific signal throughout the growing season, reducing the noise on the signal from other land cover or crop types [38]. In the United States (US), the US Department of Agriculture (USDA) generates a yearly national Cropland Data Layer (CDL) since 2007 [39] and Canada provides yearly national Annual Crop Inventory Maps (ACIM) since 2009 [40]. These masks are provided at the end of the growing season and no crop type masks are available for other countries. Therefore, generally EO-based agriculture models use static cropland or crop type masks.

The flagship moderate resolution NASA mission Landsat, with data going back to the 70s, was long used for agriculture monitoring, but with limitations mainly due to its low temporal resolution of 16 days. Coupled with the frequency of cloud cover, the revisit time for some regions is often worse. A number of studies have fused Landsat with MODIS data [41–43], and combined Landsat data with biophysical models [44, 45], leading to varying results in terms of errors as they are still constrained by the low temporal frequency of Landsat imagery. The launch of the ESA optical moderate resolution missions Sentinel-2A in 2015 and Sentinel-2B in 2017 have been revolutionary for the moderate agriculture monitoring. The increased temporal coverage and the new technologies offered by the Sentinel systems and their combination with NASA sensors, provides new opportunities for high temporal frequency moderate resolution remote sensing, enabling a new generation of agriculture products to be generated. Specifically, with the Sentinel-2A and -2B fusion with Landsat, it is now possible to achieve a temporal resolution of three to five days globally. In fact, recent studies leverage the combination of these satellites to address crop yield assessment at field scale [46–48]. Yet, simply having synergistic sensors on orbit is not sufficient for end users; the data products themselves must also be processed in such a way as to ease preprocessing and analysis burden. The Harmonized Landsat/Sentinel-2 (HLS) project [49] developed by NASA provides a surface reflectance product that combines observations from USGS/NASA's Landsat-8 (LS8) and ESA's Sentinel-2 (S2) satellites at moderate spatial resolution (30 m). The main goal is to provide a unique dataset based on both satellites' data to improve the revisit time to three to five days depending on the latitude. Along with a common atmospheric correction algorithm [50], geometric resampling to 30 m spatial resolution and geographic registration [49], the product is also corrected for Bidirectional Reflectance Distribution Function (BRDF) effects and band pass adjustment. Besides, the Sen2like tool [51] developed by ESA will provide analysis ready Harmonized LS8 and S2 data/products to the user. Using the S2 tiling system, the sen2like tool processes S2 Level-1 products and LS8 Level-1

products and create a harmonized surface reflectance data stack at 10 m spatial resolution. Working on the same baseline principles as NASA HLS initiative, geometric, radiometric and image processing algorithms are applied. Recent studies took advantage of Landsat and S2 data to address crop yield assessment at a moderate spatial resolution [52, 53].

Recent advances in data acquisition and processing (e.g., cloud computing) are making possible the development of global high-to-moderate resolution data sets (10–30 m). Such global time series data will permit improved mapping of crop type, crop area and vegetation properties essential for regional implementation of monitoring strategies. Higher temporal frequency from multiple high-to-moderate resolution satellites will also provide a better characterization of agronomic growth stages, with the consequent improvement of crop production modeling accuracy.

3 Time Series Processing for Crop Seasonality Monitoring

3.1 Gap-Filling

An essential step for being able to use EO data for further processing such as LSP calculation, is converting raw data time series into spatio-temporal continuous datasets. To ensure this, gaps mostly provoked by clouds must be filled. Time series gap filling essentially refers to the prediction of missing values in time. Mostly, these missing values are located within the dataset time series, so in principle interpolation methods to fill them up would suffice. It is therefore no surprise that interpolations and fitting methods are commonly used as a first step in the time series processing. According to the recent review by [8], gap filling methods can be categorized into: (1) smoothing and empirical methods, (2) data transformations, and (3) curve fitting methods. From these three categories, the curve fitting methods are the most commonly used, with double logistic curves being a popular method for seasonality estimation [54–56]. This family of methods has expanded rapidly in the last few years with the emergence of adaptive machine learning regression algorithms [57]. See also [57, 58] for a quantitative evaluation of these methods. Some machine learning methods proved to be particularly attractive; not only because of achieving higher accuracies when validated against a reference image, but also because of additional properties such as delivering uncertainty estimates (e.g. Gaussian processes regression: GPR). Most of these methods have been recently implemented into an in-house developed graphical user interface (GUI) toolbox, named DATimeS (Decomposition and Analysis of Time Series software) [57]. DATimeS has been developed to generate cloud-free composite maps from regular or irregular satellite time series. The novelty of the toolbox lies in expanding established time series gap-filling methods with a diversity of advanced machine learning fitting algorithms. An overview of the gap-filling methods is provided in Table 1.

Here, a brief description of the toolbox is provided, as it will be used in subsequent calculation of phenology indicators. In short, DATimeS is developed as a

Table 1 Interpolation methods used for gap-filling

	Gap-filling methods
Smoothing and Interpolation Methods	Linear, Polynomial, Nearest, Next, Previous, Pchp, Spline
Data Transformation	Offset + Harmonic analysis Offset + Harmonic analysis + Linear Term Offset + Harmonic analysis + Linear Term Offset + Harmonic Analysis using Sliding Window
Fitting methods (e.g., machine learning)	Bagging trees (BAGTREE) Adaptive Regression Splines (ARES) Boosting trees (BOOST) k-nearest neighbors regression (KNNR) Gaussian Process Regression (GPR) Kernel Ridge Regression (KRR) Locally-Weighted Polynomials (LWP) Support Vector Regression (SVR) Neural networks (NNIPL) Random forests (RF2) Boosting random trees (RF1) Structured Kernel Ridge Regression with linear Kernel (SKRRlin) Relevance Vector Machine (RVM) Sparse Spectrum Gaussian Process Regression (SSGPR) Structured Kernel Ridge Regression with RBF kernel (SKRRrbf) Decision trees (TREE) Variational Heteroscedastic Gaussian Process Regression (VHGPR) Double Logistic curve Whittaker

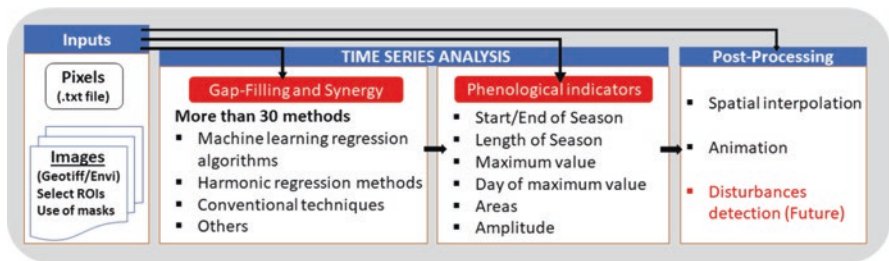


Fig. 1 Hierarchical design of DATimeS

modular toolbox that can be applied to both, set of images and discrete time series data stored in a text file. An overview of the DATimeS’ modules contained in this first version (v.1.06) is shown in Fig. 1. The core machinery of DATimeS is the “Time Series Analysis” module, where the gap-filling methods can be selected, and subsequent phenology indicators can be computed. The user may choose whether to incorporate the smoothing function prior to the parameter estimation. Although a

prior smoothing step may help in finding general patterns, it must be remarked that most fitting methods perform a time series anyhow, smoothing along with the fitting prediction. Before starting the gap-filling procedure, a compulsory step is to define the output time settings, i.e., the days to which cloud-free interpolated images will be generated (e.g., every 10 days). These composite products from operational land missions (e.g., AVHRR, MODIS, SPOT Vegetation (VGT)) are commonly used for subsequent LSP calculation [25, 59–61].

3.2 LSP Calculation

A next step involves the calculation of the phenology indicators from the prepared cloud-free time series data, i.e., the LSP metrics. Numerous studies have dealt with the retrieval of phenological phases from remotely sensed data [55, 62–65]. LSP metrics quantification over croplands is widely used for yield estimation, or to improve management and timing of field works (planting, fertilizing, irrigating, crop protection or harvesting) [66, 67]. Distinct LSP metrics may be of interest to the scientific community, private companies and farmers, such as dates of start and end of the growing season (SOS and EOS, respectively), maximum peak, seasonal amplitude defined between the base level and the maximum value for each individual season, length of the season, etc. [38, 68]. These LSP metrics are extremely sensitive to changes in vegetation cycles related to multiple factors such as climate anomalies or extreme weather events, which can have a profound impact in the agricultural production [69–71]. Hence, estimating LSP metrics is a convenient way to summarize seasonal information in a few comprehensive quantitative descriptors. However, it must be taken into account that these metrics are sensitive to the processing data characteristics or methods used (e.g., gap-filling method, pixel size, time period of the time series). Therefore, outputs must be carefully analyzed (see also review in [8]), as will be further demonstrated in the case study.

In practice, LSP metrics are recommended to be derived after the interpolation step so that cloud-free composite images are created, and trends become evident for easy phenological metrics derivation. For this reason, DATimeS recommends LSP estimation as the next logical processing module after the gap-filling module, even if going directly to this step is also possible. In this module, the whole time series is first analyzed looking for possible multiple growing seasons.

Then, each individual season is processed separately to estimate the phenological indicators (e.g., SOS and EOS) based on conventional threshold methods, analogous to [68, 72–75]. The computational routine for LSP calculation follows multiple steps. It runs pixelwise, and for each pixel it: (1) extracts the time series, (2) identifies automatically individual growing seasons within each year, (3) locates specific points within the growing season (e.g., SOS, EOS, peak), (4) computes seasonal integrals (area under the curve between SOS and EOS) and (5) stores the estimates in output ENVI or Tiff files. Three alternative methods have been implemented to calculate the SOS/EOS: (1) seasonal, (2) relative and (3) absolute amplitude. In the

former case, the SOS/EOS are identified where the left/right part of the curve reaches a fraction of the seasonal maximum amplitude along the rising/decaying part of the curve. The second approach is similar to the previous one, but now a mean amplitude is estimated considering the minimum/maximum values of all seasons. Consequently, the SOS/EOS correspond to dates where the curve reaches a specific percentage of the reference amplitude. In the latter method, the SOS/EOS are determined when each growing season reaches the same fixed value.

4 Demonstration Cases Time Series Processing

Having outlined the main principles of (1) EO missions dedicated to crop monitoring, (2) gap-filling methods, and (3) LSP calculation, this section provides some time series demonstration cases with temporal data coming from the currently most successful optical missions at low and high spatial resolution, i.e. MODIS and S2 acquisitions. The study focuses on the trade-off between revisit time and spatial resolution of each sensor and is carried out over two agricultural landscapes of the US, each one characterized by the presence of a different dominant crop type with specific phenological dynamics: winter wheat and corn.

4.1 Study Area and Data Acquisition

The US is one of the main producers and exporters of corn and wheat globally. In 2016 the US was the leading wheat exporting country, shipping 14.8% of global wheat exports¹. Wheat is produced in almost every state in the United States and winter wheat varieties dominate US production, representing between 70% and 80% of the total wheat production. The winter wheat is planted in the fall and harvested during June-July. Generally, wheat is rain-fed and just 7% of the national production is irrigated. The main wheat class is Hard Red Winter Wheat, which is grown primarily in the Great Plains, with Kansas being the largest producing state. Besides, the US is a major player in the world corn trade market, with between 10% and 20% of its corn crop exported to other countries. Corn is grown in most U.S. States, but production is concentrated in the Heartland region (including Illinois, Iowa, Indiana, eastern portions of South Dakota and Nebraska, western Kentucky and Ohio, and the northern two-thirds of Missouri). Iowa and Illinois, the top corn-producing States, typically account for about one-third of the U.S. crop. The corn is planted during April-June and is harvested during September-November.

With the aim of performing a fair comparison of multispectral spatiotemporal information carried by high- and low spatial resolution multispectral imageries, i.e. S2 and MODIS, over corn and winter wheat, the Crop Data Layer (CDL) yearly

¹<http://www.worldstopexports.com/wheat-exports-country/>

produced by the National Agricultural Statistics Service (NASS) of the US Department of Agriculture (USDA) was analyzed, and selected two S2 tiles representative of each crop type were selected.

4.1.1 Crop Data Layer

The Crop Data Layer (CDL) is distributed by NASS since 2008 at 30 m as part of the official archive of county-level statistics on yield, area harvested and production that are available from the USDA National Agricultural Statistics Service (NASS) Quick Stats database². It is a rasterized land cover map using field level training data from extensive ground surveys, farmer reports provided to the US Farm Service Agency (FSA), and remotely sensed data from Landsat Thematic Mapper (TM), Landsat Enhanced Thematic Mapper (ETM+) and Advanced Wide Field Sensor (AWiFS). These data are used in a decision tree classifier in order to produce a land cover classification that distinguishes between different crop types, including winter wheat [39, 76].

4.1.2 MODIS and Sentinel-2 Surface Reflectance Time-Series

The time span chosen for the study was the year 2019 due to the availability in Google Earth Engine (GEE) [77] of S2 surface reflectance images over the US from December 2018 on. The first tile chosen is 11TLM, which is located in North West of US, in the South of Washington and contains mainly winter wheat cultivated areas. The second one is 15TVH, centered in North Iowa, with essentially corn and soybean crops. S2 data were downloaded from GEE in UTM projective coordinates. Limited by the spatial resolution of CDL, S2 information distributed at 20 m were gathered. Aside from the crop-of-interest spatial density, a second criterion for the selection of the two areas was their medium frequency level of cloudiness estimated by analyzing MODIS daily cloud mask. This way, the main advantages and drawbacks of the shorter revisit time of coarse resolution MODIS imagery against the longer revisit time of high resolution S2 acquisitions can be assessed. Details about the spatial properties of the test sites are summarized in Fig. 2. The nine classes in the legend correspond to the most frequent classes within the two test-sites, among the 134 provided by USDA [78]. Tile 15TVH is essentially made up of two main classes, corn and soybeans; tile 11TLM presents a more heterogeneous scenario, with winter wheat being the dominant crop class after pasture. The landscape is further characterized by shrubland, but crops as spring wheat, alfalfa and potatoes are also cultivated. Grey and blue colors indicate urban and water areas, respectively.

The analysis of MODIS time series was based on MODIS daily surface reflectance Collection 6 data (MOYD09GQ) distributed by the Land Processes Distributed

²http://www.nass.usda.gov/Quick_Stats/

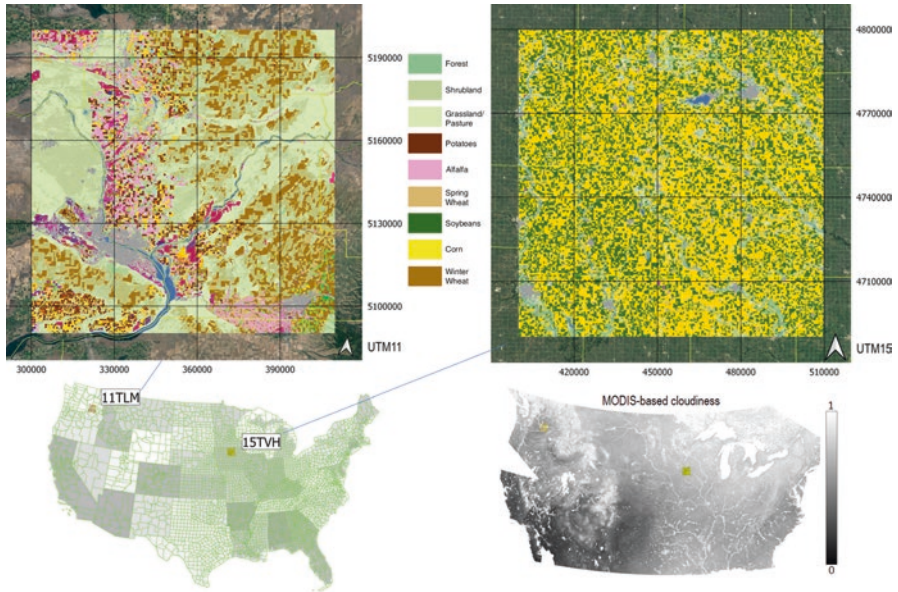


Fig. 2 USDA land cover map of 2019 over S2 footprint @30m for tiles 11TLM (left) of Washington and 15TVH (right) of Iowa. The legend details the main classes within the two tiles, among the 134 defined by USDA. Green lines and greyish areas define US Counties and States limits, respectively. The cloudiness map along 2019 was estimated as percentage of per pixel MODIS cloudy acquisitions

Active Archive Center³ (LPDAAC), which are gridded in the sinusoidal projection at 250m resolution. Additionally, the product MOYD0 was used 9GA to extract the geometry of observation illumination of each image. Since the nominal 250 m MODIS resolution decreases for the off-nadir observations and due to inaccurate registration [79], the 250 m surface reflectance was re-scaled to 1 km spatial resolution to mitigate that effect by aggregating 4×4 pixels. The wide swath MODIS sensor allows for near global coverage of the Earth every day. However, it has a 16-day repeat cycle, which means that every day the geometry of observation is different and can include View Zenith Angles (v) of up to 65 degrees. As a consequence, the surface reflectance that is defined for a given geometry of observation-illumination has different values every day. In order to normalize the BRDF effects on the surface reflectance, we used the VJB method [80, 81]. This method uses longer compositing periods (five years in [80]), than the MCD43 product (16 days) [82], which reduces the noise in the normalized reflectance time series [83]. In this study, the nadir BRDF parameters at 1 km spatial resolution using the most recent five years (2012–2016) were derived.

³https://lpdaac.usgs.gov/dataset_discovery/modis/modis_products_table

Table 2 MODIS Terra/Aqua and S2A/B imagery information over the two test-sites

Sensor	Start date	End date	Number of images	Full coverage orbit	Partially coverage orbit	Spatial resolution
MODIS T/A	1/1/2018	31/12/2019	730	–	–	1 km
S2A/B 11TLM	13/12/2018	10/01/2020	244	113	70/13	20 m
S2A/B 15TVH	13/12/2018	10/01/2020	166	69	112	20 m

By using the daily surface reflectance (from both Aqua and Terra) and its angular conditions during the five-year period considered, the variables that define the BRDF shape (V and R in Equation (1)) are derived using the approach proposed by [81]. The MODIS dataset consists of daily acquisitions covering the whole US territory during 2018 and 2019. For S2, a total amount of 237 and 158 partially cloudy or cloud-free images was collected for 11TLM and 15TVH, respectively. Despite the nominal revisit time of S2 being five days, 11TLM is fully covered by orbit 113 and partially covered by orbits 70 and 13, whereas 15TVH is fully covered by orbit 69 and partially covered by only orbit 112. This explains the different number S2 images. Details about the dataset are reported in Table 2.

4.2 Time Series Processing Over Croplands

As pointed out in Sect. 2, the main disadvantage of coarse to moderate resolution sensors is the spectral mixing from different land cover types and crops. In order to characterize the degree of homogeneity of coarse resolution pixels, the higher spatial resolution information provided by CDL map and S2 imagery can be exploited. First, a common coordinates' reference must be defined to allow establishing a pixel-to-pixel correspondence among the different information sources. MODIS data were cropped over S2 tiles 11TLM and 15TVH, projected to their corresponding UTM reference at 20 m using the nearest-neighbor interpolation, and finally aggregated at 1 km. Similarly, CDL maps were projected onto S2 UTM reference at 20 m.

The interpolated CDL was then used to calculate the percentage of each land cover class within each MODIS 1 km pixel. A qualitative description of the homogeneity of MODIS pixels is given in the 1 km land cover maps shown in images (a) and (b) of Fig. 3. For their generation, the 3 most likely classes at pixel level were taken into account. Denoting them ordered by probability as Cl_1 , Cl_2 and Cl_3 , the RGB composite was obtained by weighing the color coding of the three classes with the corresponding percentages. The visual comparison of the land cover maps at 20 m (Fig. 2) and 1 km indicates that a dominant class can be still identified at MODIS scale. Yet, the less saturated colors point out the presence of a non-negligible class mixing. The higher the mixing, the more relevant the difference between

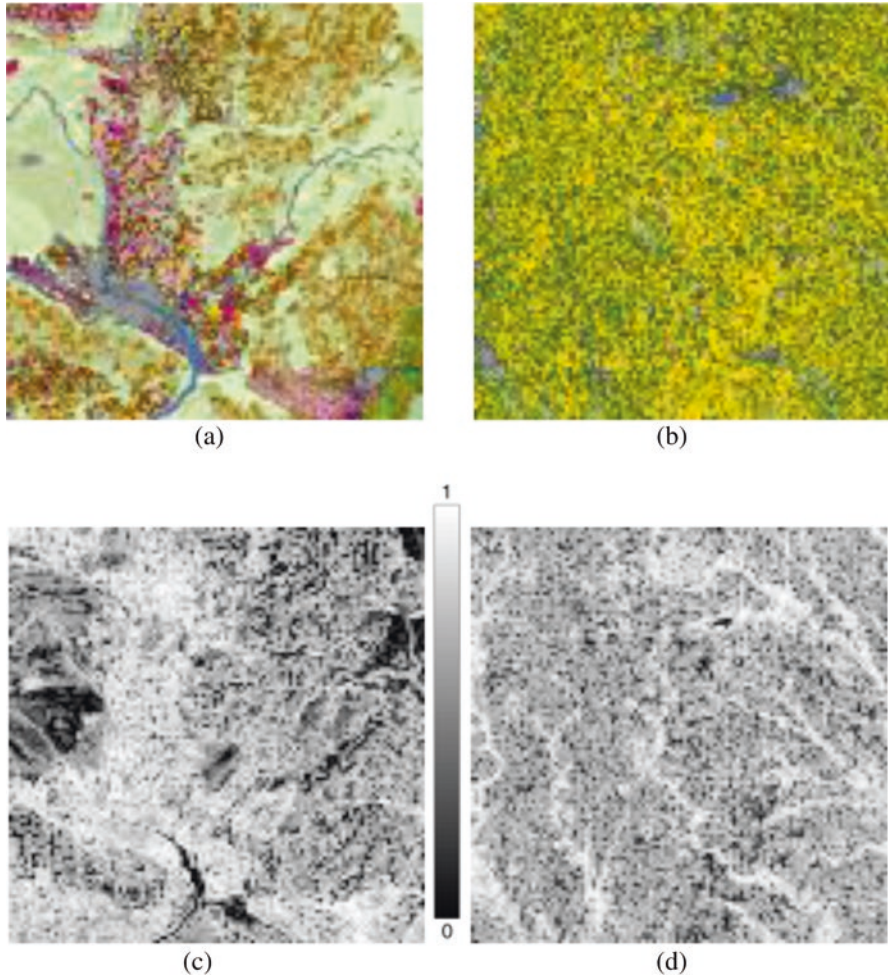


Fig. 3 Synthetic Land cover map @1km of 11TLM (a) and 15TVH (b) tiles based on USDA land cover product @30m weighted by the probability of classes Cl_1 , Cl_2 and Cl_3 within MODIS pixels. In (c) and (d) the corresponding GSI maps are showcased

MODIS and S2 spectra is. A quantitative estimation of this mixing effect is provided by the Gini-Simpson Index (GSI) [84, 85]. The GSI essentially quantifies how many different types of classes the pixel of interest contains, and is computed as the complement of the sum of squared N-member fractions of classes:

$$GSI(x,y) = \sum_{i=1}^{N_c} 1 - p_i(x,y)^2 \quad (1)$$

where (x, y) denotes the coordinates of MODIS pixel's center, N_c is the total number of CDL classes within the pixel and p_i is the fraction of the area covered by the i^{th}

class. The result obtained for the area corresponding to the two S2 tiles are shown in Fig. 3c, d. The closer GSI to zero, the purer the pixel is, i.e. a dominant class characterizes the pixel. Conversely, a higher GSI denotes a heterogeneous 1 km pixel where multiple classes are present with comparable percentages. Over the latter ones, the interpretation of coarse resolution imagery deserves special attention, as the information they contain cannot be transferred directly to individual classes. To clarify this concept, we use the Difference Vegetation Index (DVI).

DVI is a non-normalized parameter simply defined as the difference between the near-infrared and the red bands, with the main advantage to describe the evolution in time of crop phenology avoiding saturation effects often detected with other normalized indexes such as NDVI [86]. Accordingly, five DVI time series at 1 km from the two imagery sources were generated. The first two ones are the MODIS DVI from the BDRF-corrected MODIS, and the S2 DVI obtained by simply upscaling the S2 product to 1 km. Besides, for each 1 km pixel the three classes with the highest probability were selected and the S2 DVI value of 20 m pixels belonging to each of them separately was averaged. The corresponding DVI at 1 km for pixel (x,y) at time t was hence obtained as follows:

$$DVI_{CLk}(x,y,t) = \frac{1}{N_{pClk}} \sum_{i=1}^{N_{pClk}} DVI_{S2_{20m}}(x_i,y_i,t) \quad (2)$$

where N_{pClk} indicates the number of 20 m pixels (x_i, y_i) within the 1 km pixel centered in (x, y) and belonging to the class C_{lk} , with $k = 1, 2, 3$. Examples of the five-time series obtained for almost pure and heterogeneous pixels of corn and winter wheat are shown in Figs. 4 and 5, respectively.

In general, an analogous temporal evolution of DVI from MODIS (blue triangle) and upscaled S2 (magenta circle) images for the two crop types can be observed on both homogeneous and heterogeneous pixels, confirming both the effectiveness of the BDRF correction and the accuracy of the datasets spatial alignment. In terms of time sampling, the lower sampling rate of S2 does not seem to affect the reconstruction of the overall shape of vegetation dynamics significantly. Yet, quantitative assessments of phenology descriptors are required to estimate the real effect on vegetation characterization. As expected, over pixels characterized by GSI close to zero the coarse resolution imagery mimics faithfully the evolution of the dominant classes (blue asterisks). There, the 1 km information can be used directly to infer crop properties, being spurious contributions from the rest of classes negligible. On the contrary, pixels characterized by higher degrees of heterogeneity are not able to provide a direct description of the crop-type of interest, being the information drifted apart from the pure time series as far as it becomes less dominant within the pixels. For them, unmixing approaches are mandatory if reliable vegetation evolution is to be retrieved, and if only coarse resolution imagery is available the solution comes with accepting an additional loss of spatial details. A successful solution has been put forward in [87], where spectral unmixing is carried out with an Ordinary Least Square method at US County level and provides a unique crop-type time

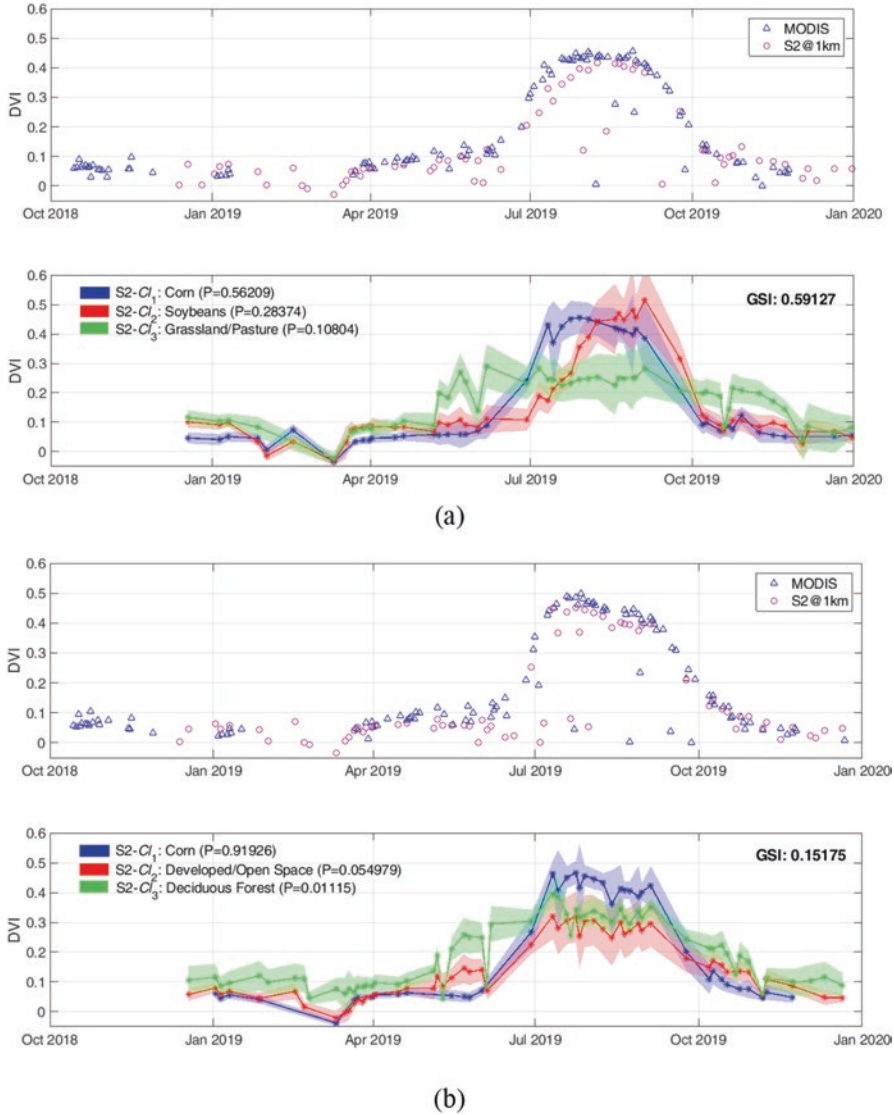
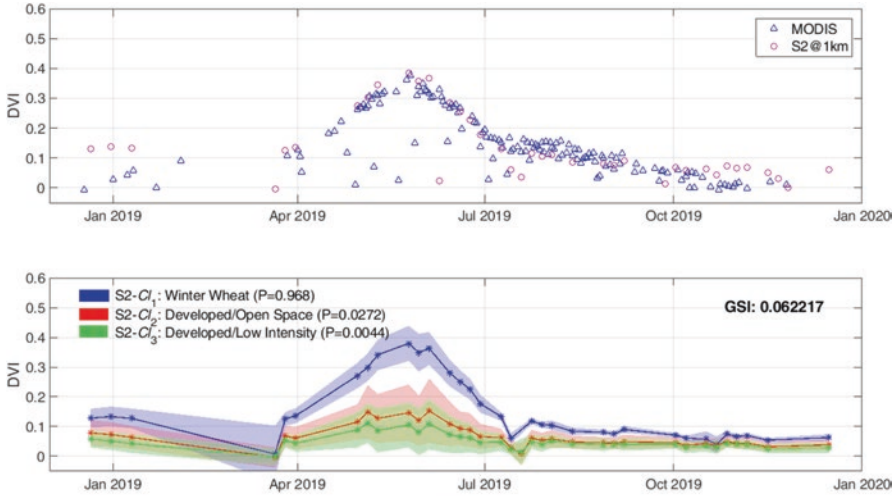


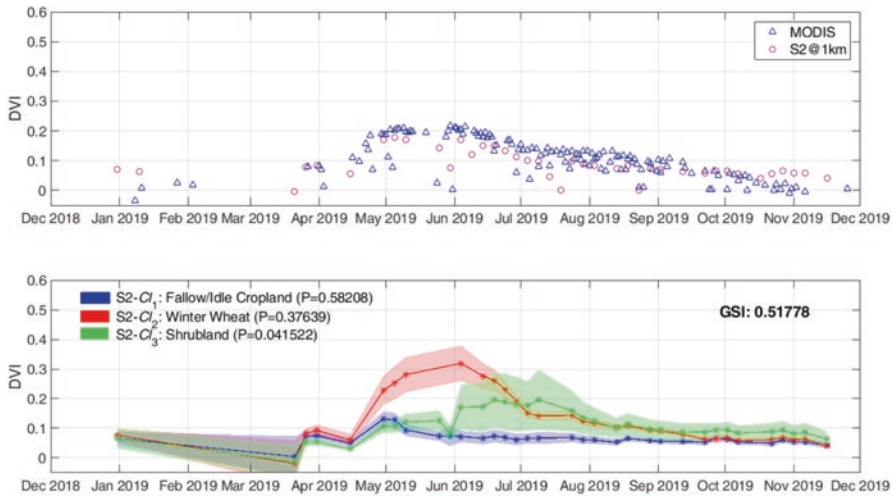
Fig. 4 DVI Time series over almost pure corn pixel (a), more abundant but not dominant corn pixel (b, c) @ 1km from MODIS, S2 and S2-based pure classes (mean value \pm 1 standard deviation with the 1 km pixel)

series at US county level. Overall, this hypothesis is fully satisfied for irrigation crops such as corn, and the county-level characterization is also representative of crop behaviors at 1 km. This can be observed in the normalized 2D histograms of DVI time series at 1 km for the tile 15TVH, shown in Fig. 6.

The corn region time series at 1 km was obtained by averaging at 1 km scale only S2 pixels labeled as corn in the USDA land cover map. A minimum crop-type



(a)



(b)

Fig. 5 DVI Time series over almost pure winter wheat pixel (a), more abundant but not dominant Winter Wheat pixel (b) @1km from MODIS, S2 and S2-based pure classes (mean value \pm 1 standard deviation with the 1km pixel)

percentage threshold of 20% was also applied to filter out noisy information. The results over the four counties entirely covered by the tile 15TVH of Iowa (Hancock, Cerro Gordo, Franklin, and Wright) show that minimum differences are detectable in the temporal evolution of the DVI, being the time sample dispersion slightly higher just during the start and end of season. Because of the corn dominance, smooth temporal profiles with a clear phenology can be detected.

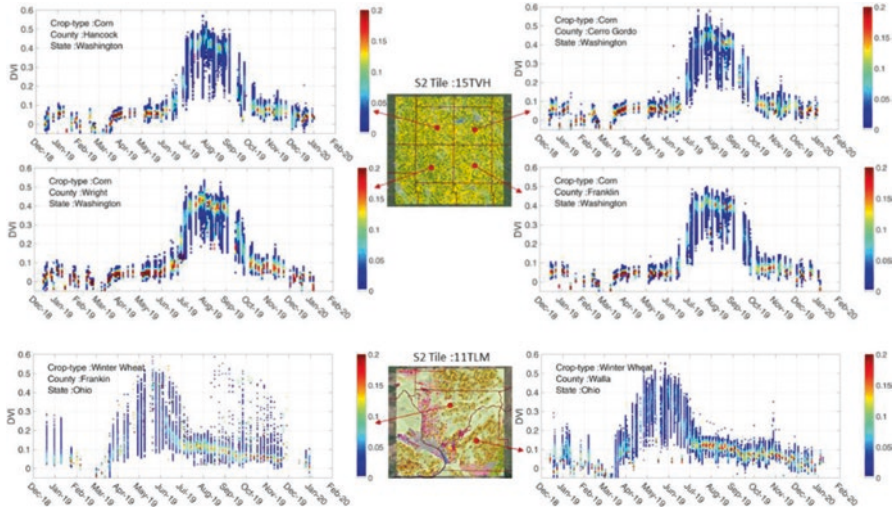


Fig. 6 Normalized 2D histograms of corn (tile: 15TVH) and winter wheat (tile: 11TLM) DVI time series at 1 km grouped by County

Conversely, when applying the same analysis to winter wheat fields of tile 11TLM, a significant spreading of time series during the whole evolution of the crop in the two counties of Washington (Franklin and Walla Walla) can be observed. Whereas the bare soil period before seeding and after harvest are stable overall the tile, the magnitude of the phenological evolution of this crop type turns out to be dependent on the specific 1 km pixel selected for the analysis. The larger spread suggests a more heterogeneous land cover with variations in phenology due to different crop types and natural vegetation. These two contrasting land covers show the case for an in depth systematic and quantitative analysis, i.e., as done by the LSP calculation.

4.3 LSP Calculation Over Croplands

The two test cases presented in the section above (e.g. see Fig. 6) have been processed by DATimeS in order to estimate the LSP metrics. To do so, first gaps due to cloud cover were filled by means of a machine learning (ML) fitting method over the temporal data. The ML algorithm Gaussian processes regression (GPR) was chosen because of excellent fitting performances (see [57, 58] for a quantitative analysis of over 20 gap-filling algorithms). As such, cloud-free DVI maps were reconstructed on a five-days basis for the year 2019. Subsequently, the LSP metrics can be reliably calculated.

The LSP metrics were calculated for the following three time series products:

Table 3 Mean and standard deviation (SD) of phenological indicators estimated from S2, S2Cl₁ and MODIS over 1km-pixel whose Cl₁ corresponded to corn (tile 15TVH). SOS, EOS and Day MV are in DOY 2019

	SOS	EOS	LOS	MV	Amp.	Day MV	Area
S2Cl₁	168.7±8.0	278.0±8.5	110.5±11.6	0.3±0.1	0.3±0.1	222.0±8.6	25.6± 4.3
S2	167.8±10.0	278.7±8.2	109.8±13.1	0.4±0.1	0.4±0.1	224.2±8.9	28.5±4.1
MODIS	164.9±11.4	279.7±5.2	113.8±12.7	0.4±0.1	0.4±0.1	225.1±6.1	31.1± 3.3

Table 4 Mean absolute deviation (MAD) and standard deviation (MSD) of MAD estimated from S2, S2Cl₁ and MODIS over 1km-pixel whose Cl₁ corresponded to corn (tile 15TVH). SOS, EOS and Day MV are in DOY 2019

	SOS	EOS	LOS	MV	Amp.	Day MV	Area
S2Cl₁ vs. S2	5.3±6.8	5.6±7.1	7.5±9.0	0.1±0.1	0.0±0.1	5.6±7.0	3.8±3.7
S2Cl₁ vs. MODIS	6.7±8.1	6.9±8.3	8.5±10.0	0.1±0.1	0.1±0.1	7.2±8.2	6.1±5.2
S2 vs. MODIS	6.4±7.9	5.6±7.0	8.0±9.5	0.0±0.1	0.0± 0.1	5.5±7.0	4.2±4.8

- **S2Cl₁**: Sentinel-2 data at 1 km obtained by averaging only pixels labeled as the dominant crop at MODIS scale, according to the CDL map. Thus, this represents the time series of pure dominant crop within each MODIS pixel;
- **S2**: Sentinel-2 data at 1 km resolution;
- **MODIS**: MODIS data at the nominal 1 km resolution.

Starting with the homogeneous corn fields dataset, general LSP results are reported in Table 3. The mean values for all the pixels are provided, as well as the associated standard deviation (SD). Considering the pure corn crop S2CL₁ as reference, it can be noticed that the S2 and MODIS data at 1km provide similar statistics, with especially the S2 product providing analogous values as the S2CL₁. The consistency can be explained by the dominance of corn fields in the S2 tile. The consistency of the LSP metrics among the three time series products can probably be better expressed by calculating the mean absolute deviation (MAD) and its dispersion, as displayed in Table 4. Differences are low, especially when comparing the S2CL₁ against the S2 product, meaning that for this more homogeneous region both S2 and MODIS datasets provide consistent temporal information.

When repeating the same exercise for the more heterogeneous landscape with winter wheat as dominant crop (Table 5), it becomes apparent that the consistency among the S2 and MODIS information somewhat degrades. This especially holds for EOS and consequent LOS with more than a month difference. On the other hand, the MV, Amp and day MV seem more robust, suggesting that the mismatch took only place in identifying the EOS. In general, the S2 dataset resembles closer the S2Cl₁ dataset, as is also quantified by the Area between SOS and EOS. The differences between S2 and MODIS are also revealed by calculating the mean absolute deviation against S2Cl₁ (Table 6); the differences with MODIS are up to two times as large as compared to S2. Altogether, it suggests that the MODIS dataset is harder

Table 5 Mean and standard deviation (SD) of phenological indicators estimated from S2, S2Cl₁ and MODIS over 1km-pixel whose Cl₁ corresponded to winter wheat (tile 11TLM). SOS, EOS and Day MV are in DOY 2019

In order to display and interpret specific spatial patterns, the maps of the LSP metrics over the two study sites turn out to be very useful	SOS	EOS	LOS	MV	Amp.	Day MV	Area
S2Cl₁	90.6±10.0	235.7±27.8	144.2±31.0	0.3±0.1	0.3±0.1	145.0±11.8	22.2±6.3
S2	88.2±8.6	220.4±30.3	131.7±31.5	0.3±0.1	0.2±0.1	145.7±14.2	20.8±7.5
MODIS	84.7±17.4	261.9±18.4	172.3±29.2	0.3±0.1	0.3±0.1	148.4±13.8	31.1±8.8

Table 6 Mean absolute deviation (MAD) and standard deviation (MSD) of MAD estimated from S2, S2Cl₁ and MODIS over 1km-pixel whose Cl₁ corresponded to winter wheat (tile 11TLM). SOS, EOS and Day MV are in DOY 2019

	SOS	EOS	LOS	MV	Amp.	Day MV	Area
S2Cl₁ vs. S2	6.0±7.8	14.3±19.7	15.7±20.3	0.0±0.1	0.1±0.1	6.6±10.2	4.7±6.2
S2Cl₁ vs. MODIS	12.6±16.4	27.5±20.1	27.1±19.4	0.1±0.1	0.1±0.1	9.3±12.7	10.7±10.8
S2 vs. MODIS	11.8±16.5	24.5±22.7	24.1±23.2	0.0±0.1	0.1±0.1	7.2±10.2	11.7±11.0

to interpret in view of the phenology of the dominant crop, winter wheat, due to the larger heterogeneity in croplands and patches of natural vegetation.

Figure 7 shows the maps for the more homogeneous region dominated by corn fields (tile 15TVH), and Fig. 8 shows the maps for the more heterogeneous landscape dominated by winter wheat (tile 11TLM). Masked areas correspond to water or urban pixels.

Starting with the corn field maps, LSP metrics maps reveal that the region is highly spatially and temporally homogeneous. This is probably best visible in the SEOS and EOS maps. All three maps show the same pattern with a pronounced SOS around DOY 165–169 (half of June) and EOS around DOY 278 (beginning of October). These numbers are in agreement with the typical corn growing patterns in the Corn belt region [88]. The maximum DVI value (MV) and amplitude show some more variation. Here slight discrepancies between S2 and MODIS can be noticed, with S2 closer to the reference maps of S2Cl₁. The thin blue line in some of the S2 maps is due to border artifacts of those S2 captures covering the tile only partially, which generate local discontinuities in time that ripple along the pixel time series and affect LSP estimation. In order to eliminate these effects, these partial acquisitions should be either filtered out from the collection or processed with morphological erosion operators to modify the boundary contours.

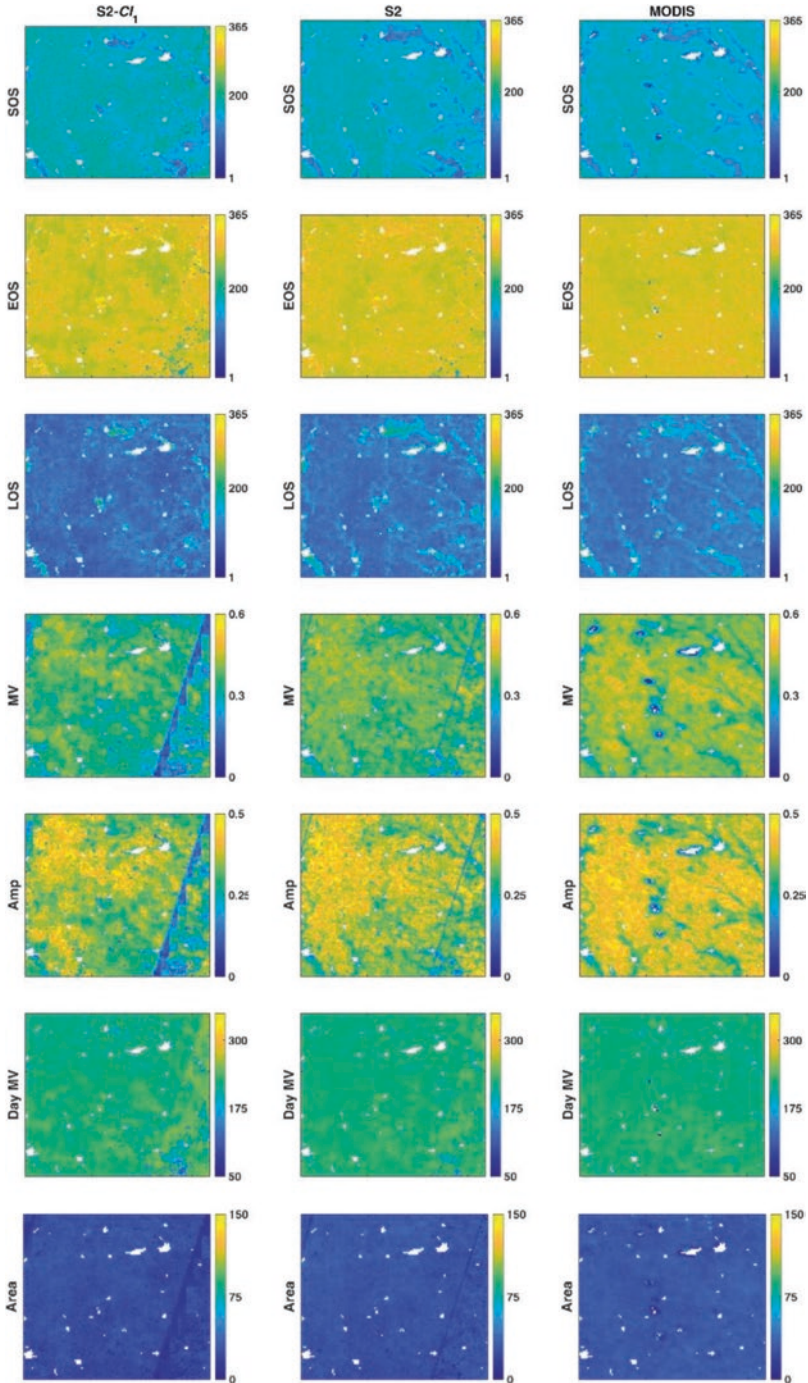


Fig. 7 LSP indicators for the year 2019 estimated from S2CI₁, S2 and MODIS at 1km-pixel over a more homogeneous agricultural region (tile 15TVH). SOS, EOS and Day MV are in DOY 2019. Masked areas correspond to water or urban pixels

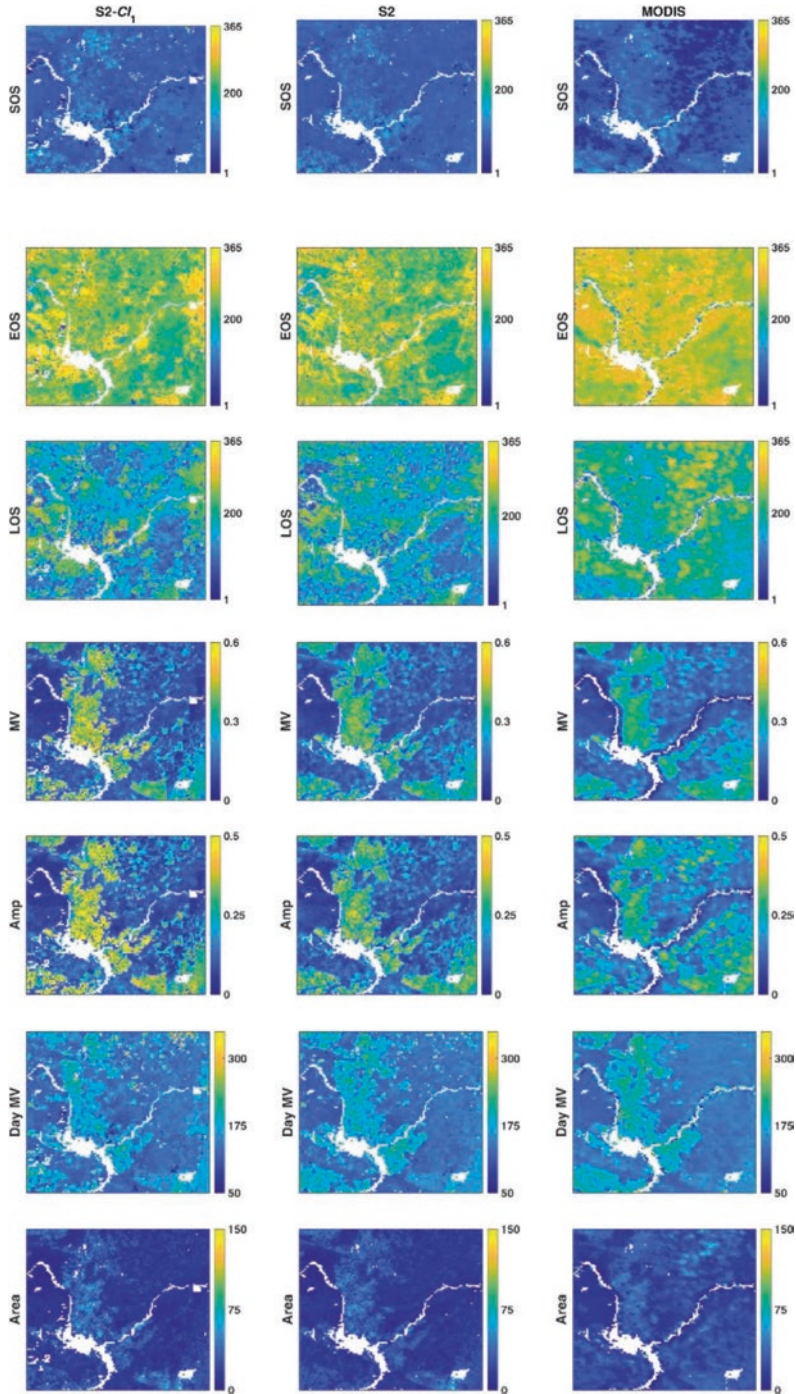


Fig. 8 Phenological indicators for the year 2019 estimated from S2CI1, S2 and MODIS at 1km-pixel over a more heterogeneous agricultural region (tile 11TLM). SOS, EOS and Day MV are in DOY 2019. Masked areas correspond to water or urban pixels

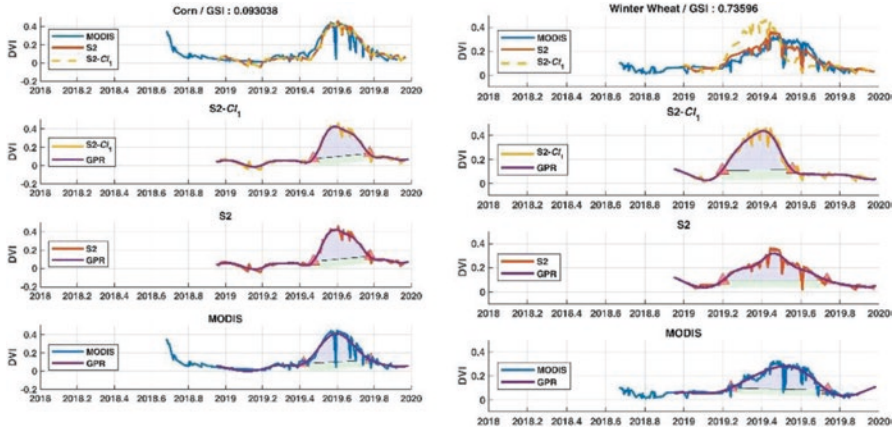


Fig. 9 Phenological indicators estimated from S2C1, S2 and MODIS for corn (low-GSI) [left] and for winter wheat (high GSI) [right]

Conversely, the more heterogeneous landscape with croplands of winter wheat but also grasslands and shrubland, display more inconsistencies in the LSP metrics maps among the three data sources. While SOS still provides consistent patterns, with a SOS around DOY 85–91 (end of March), the EOS map is remarkably less consistent. Here, S2 still provides the same patterns as S2C1₁ (EOS half of September), while the MODIS data shows a systematic later EOS (end of September). Noteworthy is that S2C1₁ maximum values (MV) and amplitude (Amp) maps provide regions with more pronounced higher values than S2 and MODIS. Both S2 and MODIS deliver smoother, more blurred maps, which again must be attributed to the greater heterogeneity in vegetation cover.

Finally, in order to improve the understanding of the LSP maps, it is worth inspecting the temporal profiles of the three data sources more closely, and relating them to the land cover heterogeneity, i.e., as expressed by the Gini-Simpson index (GSI). Figure 9 shows the temporal profiles of the three data sources for two pixels with contrasting GSA values: low for a corn field pixel and high for a winter wheat pixel. These temporal profiles help also to understand how the LSP indicators are calculated.

When having a closer look to the homogeneous corn fields (Fig. 9, left), the temporal profiles for S2C1₁, S2 and MODIS are shown in the top. A first observation is that the MODIS dataset is generally spikier, which is likely due to the higher temporal resolution, with more chances of observing inconsistencies, e.g., due to undetected cloud issues such as partial cloud cover. Regardless of the noise, the general temporal patterns of the three data products resemble closely. Accordingly, when the phenology indicators are calculated, they are alike. That is also shown in the individual calculation of SOS and EOS for each data source (see Fig. 9 underneath). For three data sources the SOS and EOS were identified at about the same dates. Conversely, for the more heterogeneous winter wheat landscape with a high GSI

(Fig. 9, right) the temporal profile of the wheat crop ($S2Cl_1$) follows a distinct pattern when compared to MODIS and S2 at 1 km patterns. Winter wheat has an earlier peak as opposed to the other phenology patterns. A closer inspection of the individual SOS and EOS calculations reveals that both MODIS and S2 express a smoother and longer pattern due to mixture of vegetation types (summer crops, grasslands or shrublands) with subsequent similar identification of SOS and EOS. The result suggests that independently of source, dataset at 1 km should be less related to crop phenology quantification and thus more care is required when interpreting this information towards crop monitoring.

5 Discussion

Having outlined a general overview of EO missions and time series processing technique applied to crop monitoring, this section provides a brief overview of a few ongoing trends with respect to satellite-based crop monitoring. They are summarized into the following topics: (1) trends in EO missions; (2) trends in gap-filling methods; (3) trends in time series data fusion, and (4) trends in time series software.

When it comes to EO imagery for crop monitoring purposes, a trade-off has to be made between spatial and temporal resolution. It does not come as a surprise that spatial resolution is a key factor to consider in phenology detection, given that medium to coarse spatial resolution imagery from sensors such as MODIS or Sentinel-3 are comprised of pixels containing a heterogeneous mosaic of multiple land cover types with varying phenological signals [8]. The impact of heterogeneity has been demonstrated here for the winter wheat case within MODIS pixels. Hence, coarse resolution data limits the extraction of specific phenological stages for specific land cover types given this sub-pixel land cover heterogeneity [89, 90]. However, in the extensive review by [8], it was also argued that the spectral-temporal signal at the coarse spatial scale is more stable over longer periods of time because the land cover composition within pixels at a resolution of 1 km or lower remains relatively static from year to year compared to higher spatial resolution pixels (e.g., S2) that detect common short-term land cover changes such as crop rotations. The study presented here just analyzes one growing season for one year, and therefore that statement cannot be confirmed, yet it is true that nominal S2 resolution (20 m) is well able to capture crop rotations (see also [57, 58]). At the same time, there is an ongoing tendency to move towards maximizing spatial and temporal resolution by making use of multiple satellites, i.e., constellations. This was first initiated with the two similar NASA satellites (Terra and Aqua) that both are equipped with the MODIS sensor [91]. The same concept of launching multiple satellites was repeated with the two S2 and Sentinel-3 constellations [92]. Progressing further along this trend, worth noting is the recent CubeSat initiative from Planet Labs, a private Earth

imaging company⁴. For the last few years Planet Labs designed and launched a constellation of CubeSats of more than 100 units. It forms the largest satellite constellation in the world that provides a complete image of Earth once per day at 3–5 m spatial resolution. Their goal is to image the entirety of the planet daily to monitor changes and pinpoint trends. With such an unprecedented richness of spatiotemporal information, first initiatives are underway to estimate phenology stages at fine spatial resolution over the US Corn Belt and so provide significant advancement to crop monitoring and precision agriculture [93].

When it comes to EO imagery time series processing, there is a strong ongoing trend towards embracing artificial intelligence methods. Particularly the machine learning (ML) fitting algorithms entered as attractive alternatives of conventional gap-filling functions. Not only may ML methods lead to more accurate reconstructions (see [57, 58] for a quantitative comparison), but they are also adaptive towards unevenly spaced data over multiple seasons. The GPR used in this chapter is of special interest, as its associated uncertainty estimate provides per-pixel information of the gap-filling confidence. Typically, the longer the gap between two consecutive input samples, the higher the uncertainty. Another interesting method is Whittaker smoother, being almost as accurate as GPR and much faster (results not shown). Its adaptive fitting performance was already earlier reported [56, 94]. It must also be remarked that the multiple provided gap-filling techniques offer, to a greater or lesser extent, different performances. Each method has its own advantages and drawbacks, which depend strongly on the characteristics of the input time series [8, 94], i.e., a method that fits well with some data can be unsuited for a different set of data points. Concerning the appropriate length of time series, even if there is no limit of amount of data, the accuracy of the time series reconstruction increases with the data size. The main limitation of the interpolation module is the high time consuming and computational cost of specific algorithms. Although not the slowest method within the family of ML fitting methods (see [57]), also GPR becomes computationally inefficient in its standard per-pixel usage when processing time series of full images, mainly due to GPR training rather than fitting step. To mitigate this computational burden, it was recently proposed to substitute the per-pixel optimization step with the creation of a cropland-based pre-calculations for the GPR hyperparameters θ [95], which basically rule the way training samples contribute to time series reconstruction depending on their distribution along the time axis. The results of this optimized approach showed that accuracies were on the same order (at most 12% RMSE degradation), whereas processing time accelerated about 90 times. The alternative option of using the same hyperparameters for all the pixels within the complete scene was further evaluated. It led to similar overall accuracies over crop areas and computational performance. Hence, it means that calculating in advance and fixing θ substantial gain in run-time can be achieved in time series reconstruction while maintaining the advantages of GPR, i.e., a high accuracy and provision of associated uncertainties.

⁴<https://www.planet.com/>

While in this chapter only single-source imagery time series datasets were addressed, among the most exciting progress in time series analysis involves multi-source data fusion. Data fusion is being increasingly used to generate time series with high temporal and spatial resolutions [41, 96]. Data fusion algorithms are expected to generate fine resolution synthetic images based on infrequent observations at fine resolution and relatively frequent coarse remote sensing data with relatively higher temporal resolution [8]. ML methods are particularly promising for data fusion, and one of the most attractive fusion methods involves the multi-output (MO) version of GPR (MOGPR). This MOGPR approach was firstly introduced in [58] to fuse optical (S2) and radar (Sentinel-1) data for improved spatiotemporal reconstruction of vegetation products such as leaf area index (LAI). This approach proved to be particularly advantageous for long gapped time series, such as prolonged cloud cover, where optical data alone notoriously fails. Hence, the data from cloud-penetrating radar technology kicks in as complementary information, although the relationship between radar and vegetation phenology is less obvious, and strongly depends on structural properties. The absolute novelty of the solution proposed in [58] is that the parameters of the trained model implicitly predict the meaningfulness of any fusion approach: they quantify the amount of information shared between the two-time series and rule the interaction of low- and high-frequency GPs for output reconstruction. Moreover, the LAI data gap filling described in [58] is only one example of MOGPR possible applications. In fact, with MOGPR multiple datasets can be fused, so to say, that is not restricted to two data sources. Any set of time series collection can be entered into the MOGPR, i.e., the use of variables from multiple optical and radar data sources, coming from multiple satellite missions, e.g., Landsat, SPOT, the Sentinels, MODIS, can be envisaged, as long as they all share a certain amount of information and are georeferenced on a common grid. This data is nowadays easily accessible on cloud-based platforms such as the Google Earth Engine. Accordingly, in the present era of freely available, continuous multi-source satellite data streams, there is no doubt that fused time series processing will become indispensable in producing accurate cloud-free data and subsequent vegetation phenology monitoring.

Finally, to the benefit of the broader community and users in the agricultural sector, another interesting trend is that increasingly dedicated software packages become available for image time series processing and phenology-related studies. As reviewed by [8], the best known, and first software package is TIMESAT [68]. Subsequent software packages are variations and extensions of it or written in other (open-source) languages, such as: Phenological Parameters Estimation Tool (PPET [97]), enhanced TIMESAT [98], TimeStats [99], Phenosat [100], HANTS [101], CropPhenology [102] and QPhenoMetrics [103]. These software tools provide free functionalities for the reconstruction of time series data and extraction of phenological information customized with a number of user-defined input parameters based on time series data (e.g., vegetation indices). They are applicable in data reconstruction providing multiple common data gap-filling methods like logistic models, Savitzky–Golay, asymmetric Gaussian functions, piecewise regression, Fourier transforms etc. and generally perform well in general LSP extraction (e.g.,

SOS, EOS) providing common extraction methods, e.g., threshold method and inflection method [8]. It must hereby be remarked that all these software packages include the same established gap-filling algorithms. Apart from being equipped with these algorithms, the newly presented DATimeS software package [57] complements with a suite of versatile ML fitting algorithms. In comparison to other time series software packages, DATimeS is state of the art, through the: (1) ability to process unevenly spaced satellite image time series; (2) possibility to select over multiple ML fitting methods for time series prediction (some methods include associated uncertainties, e.g., GPR); (3) option to fuse multiple data sources with MOGPR, and (4) provision and analysis of phenological indicators over multiple growing seasons.⁵

6 Conclusions

Satellite imagery has become an essential source of information to enable monitoring agricultural lands. Specifically, optical data from EO image time series at high temporal resolution can assist in seasonal crop monitoring, as it provides key information about vegetation growing stages over large areas. In this chapter, the ongoing trends in image time series processing for the extraction of information about land surface phenology (LSP) metrics to quantify the key moments of the crop growing season is discussed. Identified trends go in the directions of: (1) a tendency towards constellation of multiple satellites to reach both a high spatial and temporal resolution; (2) adopting machine learning algorithms for fitting multi-year and irregular time series data sources; (3) time series fusion of multiple data sources, and (4) development of dedicated software packages. With the unprecedented availability of EO data and advanced image processing methods, these trends eventually lead to improved quantification of LSP metrics, e.g., start and end of season, but also metrics more related to crop biomass or yield, such as amplitude and area. By making use of the newly developed DATimeS toolbox, the LSP calculation for time series of MODIS and S2 data at 1 km resolution over predominantly (1) homogeneous and (2) heterogeneous agricultural landscapes has been carried out. It is concluded that LSP metrics can be consistently calculated and related to the dominant crop type over a homogeneous landscape. Conversely, heterogeneous regions show some discrepancies in the LSP metrics, which may be a consequence of the more complex landscape with varying phenological behaviors of croplands and natural vegetation, combined with the different temporal resolution of the two sensors analyzed and the role of cloud cover herein. Altogether, given the extraordinary flexibility of current processing algorithms and toolboxes, it can be safely concluded that the same level of maturity is reached in exploiting optical EO data in the temporal domain as in the spatial and spectral domains.

⁵The toolbox can be freely downloaded at <https://artmootoolbox.com/>

Acknowledgments This chapter was funded by the European Research Council (ERC) under the ERC-2017-STG SENTIFLEX project (grant agreement 755617) and supported by the Action CA17134 SENSECO (Optical synergies for spatiotemporal sensing of scalable ecophysiological traits) funded by COST (European Cooperation in Science and Technology, www.cost.eu).” Belen Franch and Santiago Belda were also supported by the program Generacio Talent of Generalitat Valenciana (CIDEGENT/2018/009 and SEJIGENT/2021/001, respectively), and Jochem Verrelst by Ramón y Cajal Contract (Spanish Ministry of Science, Innovation and Universities).

References

1. Thomas F Stocker, Dahe Qin, Gian-Kasper Plattner, M Tignor, Simon K Allen, Judith Boschung, Alexander Nauels, Yu Xia, Vincent Bex, and Pauline M Midgley. Climate change 2013: The physical science basis, 2014.
2. ESA. ESA’s living planet programme: Scientific achievements and future challenges. Scientific Context of the Earth Observation Science Strategy for ESA, 2015.
3. Michele Chevrel, MICHEL Courtois, and G Weill. The SPOT satellite remote sensing mission. *Photogrammetric Engineering and Remote Sensing*, 47:1163–1171, 1981.
4. Alfredo Huete, Kamel Didan, Tomoaki Miura, E Patricia Rodriguez, Xiang Gao, and Laerte G Ferreira. Overview of the radiometric and biophysical performance of the MODIS vegetation indices. *Remote sensing of environment*, 83(1–2):195–213, 2002.
5. Xiaoyang Zhang, Mark A Friedl, Crystal B Schaaf, Alan H Strahler, John CF Hodges, Feng Gao, Bradley C Reed, and Alfredo Huete. Monitoring vegetation phenology using modis. *Remote sensing of environment*, 84(3):471–475, 2003.
6. Stephen H Boles, Xiangming Xiao, Jiyuan Liu, Qingyuan Zhang, Sharav Munkhtuya, Siqing Chen, and Dennis Ojima. Land cover characterization of Temperate East Asia using multi-temporal VEGETATION sensor data. *Remote Sensing of Environment*, 90(4):477–489, 2004.
7. Wouter Dierckx, Sindy Sterckx, Iskander Benhadj, Stefan Livens, Geert Duhoux, Tanja Van Achteren, Michael Francois, Karim Mellab, and Gilbert Saint. PROBA-V mission for global vegetation monitoring: standard products and image quality. *International Journal of Remote Sensing*, 35(7):2589–2614, 2014.
8. Linglin Zeng, Brian D Wardlow, Daxiang Xiang, Shun Hu, and Deren Li. A review of vegetation phenological metrics extraction using time-series, multispectral satellite data. *Remote Sensing of Environment*, 237:111511, 2020.
9. Sophie Moulin, Laurent Kergoat, Nicolas Viovy, and Gerard Dedieu. Global-scale assessment of vegetation phenology using NOAA/AVHRR satellite measurements. *Journal of Climate*, 10(6):1154– 1170, 1997.
10. Aaron Moody and David M Johnson. Land-surface phenologies from AVHRR using the discrete fourier transform. *Remote Sensing of Environment*, 75(3):305–323, 2001.
11. Benjamin W Heumann, JW Seaquist, Lars Eklundh, and Per Jönsson. AVHRR derived phenological change in the Sahel and Soudan, Africa, 1982–2005. *Remote sensing of environment*, 108(4):385–392, 2007.
12. Douglas E Ahl, Stith T Gower, Sean N Burrows, Nikolay V Shabanov, Ranga B Myneni, and Yuri Knyazikhin. Monitoring spring canopy phenology of a deciduous broadleaf forest using MODIS. *Remote Sensing of Environment*, 104(1):88–95, 2006.
13. Brian D Wardlow and Stephen L Egbert. Large-area crop mapping using time-series MODIS 250 m NDVI data: An assessment for the us central great plains. *Remote sensing of environment*, 112(3):1096–1116, 2008.
14. M. Drusch, U. Del Bello, S. Carlier, O. Colin, V. Fernandez, F. Gascon, B. Hoersch, C. Isola, P. Laberinti, P. Martimort, A. Meygret, F. Spoto, O. Sy, F. Marchese, and P. Bargellini.

- Sentinel2: ESA's Optical High-Resolution Mission for GMES Operational Services. *Remote Sensing of Environment*, 120:25–36, 2012.
15. C. Donlon, B. Berruti, A. Buongiorno, M.-H. Ferreira, P. Féménias, J. Frerick, P. Goryl, U. Klein, H. Laur, C. Mavrocordatos, J. Nieke, H. Rebhan, B. Seitz, J. Stroede, and R. Sciarra. The Global Monitoring for Environment and Security (GMES) Sentinel-3 mission. *Remote Sensing of Environment*, 120:37–57, 2012.
 16. D. Labate, M. Ceccherini, A. Cisbani, V. De Cosmo, C. Galeazzi, L. Giunti, M. Melozzi, S. Pieraccini, and M. Stagi. The PRISMA payload optomechanical design, a high performance instrument for a new hyperspectral mission. *Acta Astronautica*, 65(9–10):1429–1436, 2009.
 17. T. Stuffer, C. Kaufmann, S. Hofer, K.P. Farster, G. Schreier, A. Mueller, A. Eckardt, H. Bach, B. Penné, U. Benz, and R. Haydn. The EnMAP hyperspectral imager-An advanced optical payload for future applications in Earth observation programmes. *Acta Astronautica*, 61(1–6):115–120, 2007.
 18. D.A. Roberts, D.A. Quattrochi, G.C. Hulley, S.J. Hook, and R.O. Green. Synergies between VSWIR and TIR data for the urban environment: An evaluation of the potential for the Hyperspectral Infrared Imager (HyspIRI) Decadal Survey mission. *Remote Sensing of Environment*, 117:83–101, 2012.
 19. S. Kraft, U. Del Bello, M. Bouvet, M. Drusch, and J. Moreno. Flex: Esa's earth explorer 8 candidate mission. pages 7125–7128, 2012.
 20. D.K. Bolton and M.F. Friedl. Forecasting crop yield using remotely sensed vegetation indices and crop phenology metrics. *Agricultural and Forest Meteorology*, 173:74–84, 2013.
 21. Y. Dong and C.Y. Peng. Principled missing data methods for researchers. *Springerplus*, 2(1):222:1– 17, 2013.
 22. M. Schwartz. *Phenology: An Integrative Environmental Science*, volume 2. Springer Netherlands, 2013.
 23. Michael A White, Forrest Hoffman, William W Hargrove, and Ramakrishna R Nemani. A global framework for monitoring phenological responses to climate change. *Geophysical Research Letters*, 32(4), 2005.
 24. B.C. Reed, M.D. Schwartz, and X. Xiao. Remote sensing phenology: Status and the way forward. *Phenology of Ecosystems Processes*, pages 231–246, 2009.
 25. Kirsten M De Beurs and Geoffrey M Henebry. Land surface phenology, climatic variation, and institutional change: Analyzing agricultural land cover change in kazakhstan. *Remote Sensing of Environment*, 89(4):497–509, 2004.
 26. Robert B Macdonald. A summary of the history of the development of automated remote sensing for agricultural applications. *IEEE Transactions on Geoscience and Remote Sensing*, (6):473–482, 1984.
 27. Belen Franch, Eric F Vermote, Jean-Claude Roger, Emilie Murphy, Inbal Becker-Reshef, Chris Justice, Martin Claverie, Jyoteshwar Nagol, Ivan Csizar, Dave Meyer, et al. A 30+ year AVHRR land surface reflectance climate data record and its application to wheat yield monitoring. *Remote Sensing*, 9(3):296, 2017.
 28. Siyuan Wang, Hang Yin, Qichun Yang, Hui Yin, Xiaoyue Wang, Yaoyao Peng, and Ming Shen. Spatiotemporal patterns of snow cover retrieved from NOAA-AVHRR LTDR: a case study in the tibetan plateau, china. *International Journal of Digital Earth*, 10(5):504–521, 2017.
 29. Martin Claverie, Jessica L Matthews, Eric F Vermote, and Christopher O Justice. A 30+ year AVHRR LAI and fAPAR climate data record: Algorithm description and validation. *Remote Sensing*, 8(3):263, 2016.
 30. Alexandre Verger, Frédéric Baret, Marie Weiss, Iolanda Filella, and Josep Peñuelas. Geoclim: A global climatology of LAI, fAPAR, and fcover from vegetation observations for 1999–2010. *Remote Sensing of Environment*, 166:126–137, 2015.
 31. Yves Julien and José A Sobrino. The yearly land cover dynamics (YLCD) method: An analysis of global vegetation from NDVI and LST parameters. *Remote sensing of environment*, 113(2):329–334, 2009.

32. Xiao-Peng Song, Matthew C Hansen, Stephen V Stehman, Peter V Potapov, Alexandra Tyukavina, Eric F Vermote, and John R Townshend. Global land change from 1982 to 2016. *Nature*, 560(7720):639–643, 2018.
33. Jose A Moreno Ruiz, David Riaño, Manuel Arbelo, Nancy HF French, Susan L Ustin, and Michael L Whiting. Burned area mapping time series in Canada (1984–1999) from NOAA-AVHRR LTDR: A comparison with other remote sensing products and fire perimeters. *Remote Sensing of Environment*, 117:407–414, 2012.
34. Zhen Song, Shunlin Liang, Dongdong Wang, Yuan Zhou, and Aolin Jia. Long-term record of top-of-atmosphere albedo over land generated from AVHRR data. *Remote Sensing of Environment*, 211:71–88, 2018.
35. Christopher O Justice, Eric Vermote, Jeff Privette, and Alain Sei. The evolution of US moderate resolution optical land remote sensing from AVHRR to VIIRS. pages 781–806, 2010.
36. Sergii Skakun, Christopher O Justice, Eric Vermote, and Jean-Claude Roger. Transitioning from MODIS to VIIRS: an analysis of inter-consistency of NDVI data sets for agricultural monitoring. *International journal of remote sensing*, 39(4):971–992, 2018.
37. Jude H Kastens, Terry L Kastens, Dietrich LA Kastens, Kevin P Price, Edward A Martinko, and Re-Yang Lee. Image masking for crop yield forecasting using AVHRR NDVI time series imagery. *Remote Sensing of Environment*, 99(3):341–356, 2005.
38. Belen Franch, Eric F Vermote, Sergii Skakun, Jean-Claude Roger, Inbal Becker-Reshef, Emilie Murphy, and C Justice. Remote sensing based yield monitoring: Application to winter wheat in United States and Ukraine. *International Journal of Applied Earth Observation and Geoinformation*, 76:112–127, 2019.
39. David M Johnson, Richard Mueller, et al. The 2009 cropland data layer. *Photogramm. Eng. Remote Sens*, 76(11):1201–1205, 2010.
40. T Fiset, P Rollin, Z Aly, L Campbell, B Daneshfar, P Filyer, A Smith, A Davidson, J Shang, and I Jarvis. AAFC annual crop inventory. In *2013 Second International Conference on AgroGeoinformatics (Agro-Geoinformatics)*, pages 270–274. IEEE, 2013.
41. Feng Gao, Martha C Anderson, Xiaoyang Zhang, Zhengwei Yang, Joseph G Alfieri, William P Kustas, Rick Mueller, David M Johnson, and John H Prueger. Toward mapping crop progress at field scales through fusion of Landsat and MODIS imagery. *Remote Sensing of Environment*, 188:9–25, 2017.
42. Liang Sun, Feng Gao, Martha C Anderson, William P Kustas, Maria M Alsina, Luis Sanchez, Brent Sams, Lynn McKee, Wayne Dulaney, William A White, et al. Daily mapping of 30 m LAI and NDVI for grape yield prediction in California vineyards. *Remote Sensing*, 9(4):317, 2017.
43. Lin Yan and David P Roy. Spatially and temporally complete landsat reflectance time series modelling: The fill-and-fit approach. *Remote Sensing of Environment*, 241:111718, 2020.
44. David B. Lobell. The use of satellite data for crop yield gap analysis. *Field Crops Research*, 143:56–64, 2013. Crop Yield Gap Analysis – Rationale, Methods and Applications.
45. David B Lobell, Gregory P Asner, J Ivan Ortiz-Monasterio, and Tracy L Benning. Remote sensing of regional crop production in the Yaqui valley, Mexico: estimates and uncertainties. *Agriculture, Ecosystems & Environment*, 94(2):205–220, 2003.
46. Marie-Julie Lambert, Pierre C Sibiry Traoré, Xavier Blaes, Philippe Baret, and Pierre Defourny. Estimating smallholder crops production at village level from Sentinel-2 time series in Mali’s cotton belt. *Remote Sensing of Environment*, 216:647–657, 2018.
47. YR Lai, MJ Pringle, Peter M Kopittke, Neal W Menzies, Tom G Orton, and Yash P Dang. An empirical model for prediction of wheat yield, using time-integrated Landsat NDVI. *International journal of applied earth observation and geoinformation*, 72:99–108, 2018.
48. Sergii Skakun, Eric Vermote, Belen Franch, Jean-Claude Roger, Nataliia Kussul, Junchang Ju, and Jeffrey Masek. Winter wheat yield assessment from Landsat 8 and Sentinel-2 data: Incorporating surface reflectance, through phenological fitting, into regression yield models. *Remote Sensing*, 11(15):1768, 2019.

49. Martin Claverie, Junchang Ju, Jeffrey G Masek, Jennifer L Dungan, Eric F Vermote, Jean-Claude Roger, Sergii V Skakun, and Christopher Justice. The harmonized Landsat and Sentinel-2 surface reflectance data set. *Remote sensing of environment*, 219:145–161, 2018.
50. Eric Vermote, Chris Justice, Martin Claverie, and Belen Franch. Preliminary analysis of the performance of the Landsat 8/OLI land surface reflectance product. *Remote Sensing of Environment*, 185:46–56, 2016.
51. Sébastien Saunier, Jérôme Louis, Vincent Debaecker, Thomas Beaton, Enrico Giuseppe Cadau, Valentina Boccia, and Ferran Gascon. Sen2like, a tool to generate Sentinel-2 harmonised surface reflectance products—first results with Landsat-8. In *IGARSS 2019 IEEE International Geoscience and Remote Sensing Symposium*, pages 5650–5653. IEEE, 2019.
52. F. Gao, M. Anderson, C. Daughtry, A. Karnieli, D. Hively, and W. Kustas. A within-season approach for detecting early growth stages in corn and soybean using high temporal and spatial resolution imagery. *Remote Sensing of Environment*, 242, 2020.
53. R. Fieuzal, V. Bustillo, D. Collado, and G. Dedieu. Combined use of multi-temporal Landsat-8 and Sentinel-2 images for wheat yield estimates at the intra-plot spatial scale. *Agronomy*, 10(3), 2020.
54. Pieter S.A. Beck, Clement Atzberger, Kjell Arild Høgda, Bernt Johansen, and Andrew K. Skidmore. Improved monitoring of vegetation dynamics at very high latitudes: A new method using MODIS NDVI. *Remote Sensing of Environment*, 100(3):321–334, 2006.
55. Y. Julien and J. A. Sobrino. Global land surface phenology trends from GIMMS database. *International Journal of Remote Sensing*, 30(13):3495–3513, 2009.
56. Peter M. Atkinson, C. Jeganathan, Jadu Dash, and Clement Atzberger. Inter-comparison of four models for smoothing satellite sensor time-series data to estimate vegetation phenology. *Remote Sensing of Environment*, 123:400–417, 2012.
57. DATimeS: a machine learning time series GUI toolbox for gap-filling and vegetation phenology trends detection], author=Belda, Santi and Pipia, Luca and Rivera-Caicedo, Juan Pablo and Amin, Eatidal, de Grave, Charlotte and Verrels, Jochem, Environmental Modelling and Software Journal, volume=submitted, publisher=Elsevier.
58. Luca Pipia, Jordi Muñoz-Marí, Eatidal Amin, Santiago Belda, Gustau Camps-Valls, and Jochem Verrelst. Fusing optical and SAR time series for LAI gap filling with multiooutput gaussian processes. *Remote Sensing of Environment*, 235:111452, 2019.
59. Jin Chen, Per Jönsson, Masayuki Tamura, Zhihui Gu, Bunkei Matsushita, and Lars Eklundh. A simple method for reconstructing a high-quality NDVI time-series data set based on the savitzky–golay filter. *Remote sensing of Environment*, 91(3–4):332–344, 2004.
60. R. Stockli and P.L. Vidale. European plant phenology and climate as seen in a 20-year AVHRR land-surface parameter dataset. *International Journal of Remote Sensing*, 25(17):3303–3330, 2004.
61. R. Fensholt, K. Rasmussen, T.T. Nielsen, and C. Mbow. Evaluation of earth observation based long term vegetation trends - intercomparing ndvi time series trend analysis consistency of Sahel from AVHRR GIMMS, TERRA MODIS and SPOT VGT data. *Remote Sensing of Environment*, 113(9):1886–1898, 2009.
62. Michael A. White, Kirsten M. De Beurs, Kamel Didan, David W. Inouye, Andrew D. Richardson, Olaf P. Jensen, John O’Keefe, Gong Zhang, Ramakrishna R. Nemani, Willem J. D. Van Leeuwen, Jesslyn F. Brown, Allard De Wit, Michael Schaeppman, Xioamao Lin, Michael Dettinger, Amey S. Bailey, John Kimball, Mark D. Schwartz, Dennis D. Baldocchi, John T. Lee, and William K. Lauenroth. Intercomparison, interpretation, and assessment of spring phenology in North America estimated from remote sensing for 1982 to 2006. *Global Change Biology*, 15(10):2335–2359, 2009.
63. B. Tan, J. T. Morissette, R. E. Wolfe, F. Gao, G. A. Ederer, J. Nightingale, and J. A. Pedelty. An enhanced TIMESAT algorithm for estimating vegetation phenology metrics from MODIS data. *IEEE Journal of Selected Topics in Applied Earth Observations and Remote Sensing*, 4(2):361–371, June 2011.

64. Mark Broich, Alfredo Huete, Matt Paget, Xuanlong Ma, Mirela Tulbure, Natalia Restrepo Coupe, Bradley Evans, Jason Beringer, Rakhesh Devadas, Kevin Davies, and Alex Held. A spatially explicit land surface phenology data product for science, monitoring and natural resources management applications. *Environmental Modelling & Software*, 64:191–204, 2015.
65. Elias Fernando Berra, Rachel Gaulton, and Stuart Barr. Assessing spring phenology of a temperate woodland: A multiscale comparison of ground, unmanned aerial vehicle and Landsat satellite observations. *Remote Sensing of Environment*, 223:229–242, 2019.
66. D.J. Mulla. Twenty five years of remote sensing in precision agriculture: Key advances and remaining knowledge gaps. *Biosystems Engineering*, 114(4):358–371, 2013.
67. T. Sakamoto, M. Yokozawa, H. Toritani, M. Shibayama, N. Ishitsuka, and H. Ohno. A crop phenology detection method using time-series MODIS data. *Remote Sensing of Environment*, 96(3–4):366–374, 2005.
68. J. Jönsson and L. Eklundh. TIMESAT - a program for analysing time-series of satellite sensor data. *Computers and Geosciences*, 30:833–845, 2004.
69. J.A. Sobrino and Y. Julien. Global trends in NDVI-derived parameters obtained from GIMMS data. *International Journal of Remote Sensing*, 32(15):4267–4279, 2011.
70. A.D. Richardson, T.F. Keenan, M. Migliavacca, Y. Ryu, O. Sonnentag, and M. Toomey. Climate change, phenology, and phenological control of vegetation feedbacks to the climate system. *Agricultural and Forest Meteorology*, 169:156–173, 2013.
71. C. Atzberger. Advances in remote sensing of agriculture: Context description, existing operational monitoring systems and major information needs. *Remote Sensing*, 5(2):949–981, 2013.
72. Daniel Lloyd. A phenological classification of terrestrial vegetation cover using shortwave vegetation index imagery. *International Journal of Remote Sensing*, 11(12):2269–2279, 1990.
73. Nicolas Delbart, Thuy Le Toan, Laurent Kergoat, and Violetta Fedotova. Remote sensing of spring phenology in boreal regions: A free of snow-effect method using NOAA-AVHRR and SPOT-VGT data (1982–2004). *Remote Sensing of Environment*, 101(1):52–62, 2006.
74. Michael A. White and Ramakrishna R. Nemani. Real-time monitoring and short-term forecasting of land surface phenology. *Remote Sensing of Environment*, 104(1):43–49, 2006.
75. Wen-bin Wu, Peng Yang, Hua-jun Tang, Qing-bo Zhou, Zhong-xin Chen, and Ryosuke Shibasaki. Characterizing spatial patterns of phenology in cropland of China based on remotely sensed data. *Agricultural Sciences in China*, 9(1):101–112, 2010.
76. Claire Boryan, Zhengwei Yang, Rick Mueller, and Mike Craig. Monitoring us agriculture: the US department of agriculture, national agricultural statistics service, cropland data layer program. *Geocarto International*, 26(5):341–358, 2011.
77. Noel Gorelick, Matt Hancher, Mike Dixon, Simon Ilyushchenko, David Thau, and Rebecca Moore. Google Earth Engine: Planetary-scale geospatial analysis for everyone. *Remote sensing of Environment*, 202:18–27, 2017.
78. USDA NASS. Usda-national agricultural statistics service, cropland data layer. *United States Department of Agriculture, National Agricultural Statistics Service, Marketing and Information Services Office, Washington, DC [Available at <http://nassgeodata.gmu.edu/Crop-Scape>, Last accessed September 2012.]*, 2003.
79. Fran,cois-Marie Bréon, Eric Vermote, Emilie Fedele Murphy, and Belen Franch. Measuring the directional variations of land surface reflectance from modis. *IEEE Transactions on Geoscience and Remote Sensing*, 53(8):4638–4649, 2015.
80. Eric Vermote, Christopher O Justice, and François-Marie Bréon. Towards a generalized approach for correction of the BRDF effect in MODIS directional reflectances. *IEEE Transactions on Geoscience and Remote Sensing*, 47(3):898–908, 2008.
81. Belen Franch, Eric F Vermote, José A Sobrino, and Yves Julien. Retrieval of surface albedo on a daily basis: Application to MODIS data. *IEEE Transactions on Geoscience and Remote Sensing*, 52(12):7549–7558, 2014.
82. Crystal B Schaaf, Feng Gao, Alan H Strahler, Wolfgang Lucht, Xiaowen Li, Trevor Tsang, Nicholas C Strugnell, Xiaoyang Zhang, Yufang Jin, Jan-Peter Muller, et al. First operational

- BRDF, albedo nadir reflectance products from MODIS. *Remote sensing of Environment*, 83(1–2):135–148, 2002.
83. Fran, cois-Marie Bréon, Eric Vermote, Emilie Fedele Murphy, and Belen Franch. Measuring the directional variations of land surface reflectance from modis. *IEEE Transactions on Geoscience and Remote Sensing*, 53(8):4638–4649, 2015.
 84. Aisling J Daly, Jan M Baetens, and Bernard De Baets. Ecological diversity: measuring the unmeasurable. *Mathematics*, 6(7):119, 2018.
 85. María Piles, Kaighin A McColl, Dara Entekhabi, Narendra Das, and Miriam Pablos. Sensitivity of aquarius active and passive measurements temporal covariability to land surface characteristics. *IEEE Transactions on Geoscience and Remote Sensing*, 53(8):4700–4711, 2015.
 86. C. Bacour, F. Baret, D. Béal, M. Weiss, and K. Pavageau. Neural network estimation of LAI, fAPAR, fCover and LAI×Cab, from top of canopy MERIS reflectance data: Principles and validation. *Remote Sensing of Environment*, 105(4):313–325, 2006.
 87. Belen Franch, Eric F Vermote, Sergii Skakun, Jean-Claude Roger, Inbal Becker-Reshef, Emilie Murphy, and C Justice. Remote sensing based yield monitoring: Application to winter wheat in United states and Ukraine. *International Journal of Applied Earth Observation and Geoinformation*, 76:112–127, 2019.
 88. H. Jiang, H. Hu, R. Zhong, J. Xu, J. Xu, J. Huang, S. Wang, Y. Ying, and T. Lin. A deep learning approach to conflating heterogeneous geospatial data for corn yield estimation: A case study of the US corn belt at the county level. *Global Change Biology*, 26(3):1754–1766, 2020.
 89. Jeremy Isaac Fisher, John F Mustard, and Matthew A Vadeboncoeur. Green leaf phenology at Landsat resolution: Scaling from the field to the satellite. *Remote sensing of environment*, 100(2):265–279, 2006.
 90. Katharine White, Jennifer Pontius, and Paul Schaberg. Remote sensing of spring phenology in northeastern forests: A comparison of methods, field metrics and sources of uncertainty. *Remote Sensing of Environment*, 148:97–107, 2014.
 91. J.R.G. Townshend and C.O. Justice. Towards operational monitoring of terrestrial systems by moderate-resolution remote sensing. *Remote Sensing of Environment*, 83(1–2):351–359, 2002.
 92. M. Berger, J. Moreno, J.A. Johannessen, P.F. Levelt, and R.F. Hanssen. ESA’s sentinel missions in support of Earth system science. *Remote Sensing of Environment*, 120:84–90, 2012.
 93. Hyungsuk Kimm, Kaiyu Guan, Chongya Jiang, Bin Peng, Laura F Gentry, Scott C Wilkin, Sibo Wang, Yaping Cai, Carl J Bernacchi, Jian Peng, et al. Deriving high-spatiotemporal-resolution leaf area index for agroecosystems in the us corn belt using planet labs cubesat and stair fusion data. *Remote Sensing of Environment*, 239:111615, 2020.
 94. Clement Atzberger and Paul HC Eilers. A time series for monitoring vegetation activity and phenology at 10-daily time steps covering large parts of South America. *International Journal of Digital Earth*, 4(5):365–386, 2011.
 95. Santiago Belda, Luca Pipia, Pablo Morcillo-Pallarés, and Jochem Verrelst. Optimizing gaussian process regression for image time series gap-filling and crop monitoring. *Agronomy*, 10(5):618, 2020.
 96. JJ Walker, KM De Beurs, and RH Wynne. Dryland vegetation phenology across an elevation gradient in Arizona, USA, investigated with fused MODIS and Landsat data. *Remote Sensing of Environment*, 144:85–97, 2014.
 97. Rodney D McKellip, Kenton W Ross, Joseph P Spruce, James C Smoot, Robert E Ryan, Gerald E Gasser, Donald L Prados, and Ronald D Vaughan. Phenological parameters estimation tool. 2010.
 98. Bin Tan, Jeffrey T Morisette, Robert E Wolfe, Feng Gao, Gregory A Ederer, Joanne Nightingale, and Jeffrey A Pedelty. An enhanced timesat algorithm for estimating vegetation phenology metrics from MODIS data. *IEEE Journal of Selected Topics in Applied Earth Observations and Remote Sensing*, 4(2):361–371, 2010.
 99. Thomas Udelhoven. Timestats: A software tool for the retrieval of temporal patterns from global satellite archives. *IEEE Journal of Selected Topics in Applied Earth Observations and Remote Sensing*, 4(2):310–317, 2010.

100. Arlete Rodrigues, Andre RS Marcal, and Mario Cunha. Phenology parameter extraction from timeseries of satellite vegetation index data using phenosat. In *2012 IEEE International Geoscience and Remote Sensing Symposium*, pages 4926–4929. IEEE, 2012.
101. Jie Zhou, Li Jia, Guangcheng Hu, and Massimo Menenti. Reconstruction of global MODIS NDVI time series: Performance of harmonic analysis of time series (HANTS). *Remote Sensing of Environment*, 163:217–228, 2015.
102. Sofanit Araya, Bertram Ostendorf, Gregory Lyle, and Megan Lewis. Cropphenology: An R package for extracting crop phenology from time series remotely sensed vegetation index imagery. *Ecological Informatics*, 46:45–56, 2018.
103. Lia Duarte, Ana C Teodoro, Ant´onio T Monteiro, M´ario Cunha, and Hernˆani Gon¸alves. Qphenometrics: An open source software application to assess vegetation phenology metrics. *Computers and Electronics in Agriculture*, 148:82–94, 2018